IVYSPRING INTERNATIONAL PUBLISHER

Theranostics

2018; 8(13): 3597-3610. doi: 10.7150/thno.25608

Research Paper

Cell-penetrating peptide-based nanovehicles potentiate lymph metastasis targeting and deep penetration for anti-metastasis therapy

Haiyan Hu[1,#], Jing Wang[1,#], Hong Wang[2], Tao Tan[2], Jie Li[2], Zhiwan Wang[2], Kaoxiang Sun[1,✉], Yaping Li[1,2,✉], Zhiwen Zhang[2,✉]

1. School of Pharmacy, Key Laboratory of Molecular Pharmacology and Drug Evaluation (Yantai University), Ministry of Education, Collaborative Innovation Center of Advanced Drug Delivery System and Biotech Drugs in Universities of Shandong, Yantai University, Yantai 264005, Shandong, China.
2. State Key Laboratory of Drug Research and Center of Pharmaceutics, Shanghai Institute of Materia Medica, Chinese Academy of Sciences, Shanghai 201203, China.

[#]These authors contributed equally to this work.

✉ Corresponding authors: Prof. Kaoxiang Sun (sunkaoxiang@luye.cn), Prof. Yaping Li (ypli@simm.ac.cn), and Prof. Zhiwen Zhang (zwzhang0125@simm.ac.cn). Tel/Fax: +86-21-20231979

Received: 2018.02.19; Accepted: 2018.05.04; Published: 2018.06.07

Abstract

Lymph metastasis is a vital pathway of cancer cell dissemination, and insidious lymph node metastasis increases the risk of distant cancer metastasis. Current therapies for lymph metastasis are largely restricted by limited targeting and penetration capacity. Herein, we report that an r9 cell-penetrating peptide-based cabazitaxel nanovehicle (r9-CN) displays prominent lymph metastasis targeting and deep penetration ability after intravenous injection for effective anti-metastasis therapy.

Methods: The r9-CN and CN nanovehicles were prepared by thin film dispersion, using DSPE-PEG2000 as the nano-carrier material and cabazitaxel as the model drug to fabricate r9-modified nano-micelles by self-assembly. The morphology, size, and stability in physiological solutions of r9-CN and CN were characterized. The targeting, biodistribution, deep penetration, and therapeutic efficacy of r9-CN and CN were systematically explored in vitro and in vivo.

Results: The r9-CN nanovehicle consists of homogeneous particles with a mean diameter of 13 nm and zeta potential of +0.75 mV. Compared with the nanovehicle lacking the r9 peptide (CN), r9-CN exhibits long retention and deep penetration in the tumor mass, and considerably enhances accumulation and flexible permeation in metastatic lymph nodes, thereby notably suppressing primary tumor growth, lymph node metastasis, and distant lung metastasis.

Conclusion: The cumulative findings reveal that r9-CN offers a promising delivery platform, enabling efficient lymph metastasis targeting and deep penetration for effective anti-metastasis therapy.

Key words: lymph metastasis, cell-penetrating peptide, nanovehicle, micelles, deep penetration

Introduction

Metastasis is a well-known phenomenon that results in high mortality rates for metastatic breast cancer patients [1, 2], and the lymph nodes near the original tumor are usually the first sites of tumor cell dissemination [2-5]. Once invaded by tumor cells, regional lymph nodes can act as reservoirs where cancer cells become established and from which they seed into other parts of the body [6-8]. Moreover, after surgery, the insidious activities of metastatic lymph nodes significantly increase the risk of cancer relapse and distant metastasis [5, 8, 9]. Accordingly, metastatic lymph nodes are a prime target for the efficient treatment of cancer metastasis. Recent reports have indicated that nanoscale vehicles may enable the delivery of a large variety of therapeutic agents to metastatic tumor sites, thereby providing substantial

opportunities for targeting the metastatic lymph nodes [10-13].

Many current nanovehicles are commonly administered by intra-lymphatic or local injection to target lymph node metastasis [12-21]. However, the accumulation of nanovehicles in metastatic lymph nodes via local injection has thus far been largely limited because of the high dispersion of metastases in multiple nodes, the incidence of lymph metastasis beyond the surgical area, and impaired lymph drainage in tumors, among other difficulties [11, 22-25]. Intravenous injection of chemotherapeutic agents has been extensively used in clinical cancer therapy and have demonstrated effective responses to lymph node metastasis [26, 27]. Alternatively, the intravenous administration of nanovehicles can provide a modality for systemic targeting of lymph node metastasis. However, presumably because of a blood-lymph barrier, the lymphatic system is poorly accessed via intravenous injection [6]. Worse still, the limited accumulation, short retention, and poor penetration of chemotherapeutic drugs within metastatic lymph nodes greatly restricts their interactions with cancer cells [28, 29], thereby compromising the therapeutic efficacy against lymph metastasis. Novel strategies that circumvent these issues to improve drug delivery to metastatic lymph nodes by intravenous injection are in high demand for anti-metastasis therapy.

Recently, micelles have attracted particular interest for treating metastatic lymph nodes [19, 23, 24, 30, 31]. Kataoka and colleagues examined the molecular sieving property of the blood-lymph barrier using size-controlled polymeric micelles [23, 24]. The transport from plasma to lymph was found to be highly selective, depending on the particle size of the nanovehicles, especially when the diameter was less than 30 nm [24]. Despite their arrival at the lymph metastases, the nanovehicles remained difficult to maintain in the lymph metastases sites long enough to diffuse into the interior of the tumor. Moreover, micelles are self-assembled nanovehicles that typically consist of amphiphilic block copolymers [32]. The hydrophilic polyethylene glycol (PEG) shells of micelles can effectively extend the circulation time in blood, but unexpectedly impede their internalization by cancer cells [33, 34]. The D-oligoarginine peptide (r9), a typical cell-penetrating peptide, has shown evidence of superlative efficiency for intracellular delivery and in vivo tumor targeting, but has never been explored in lymph metastasis targeting [35-39]. Therefore, the functionalization of micelles with r9 peptide can be expected to enable improved delivery efficiency to lymph metastasis sites for anti-metastasis therapy.

From this perspective, we investigated an r9 cell-penetrating peptide-based cabazitaxel (CTX) nanovehicle (r9-CN) that showed exceeding lymph metastasis targeting and deep penetration capability for effective anti-metastasis therapy (**Figure 1**).

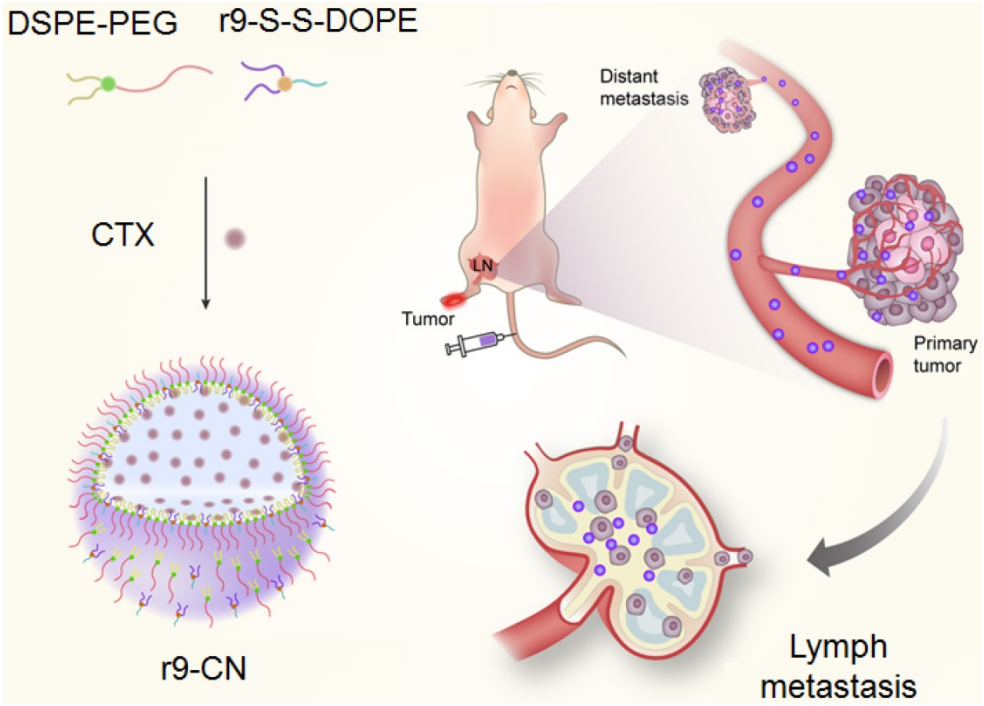

Figure 1. Schematic illustration of r9-CN-mediated preferential targeting of lymph node for effective anti-metastasis therapy. The intravenously injected r9-CN can be specifically delivered to primary tumor and lymph node metastasis sites with deep penetration capability, thereby inhibiting primary tumor growth, lymph metastasis, and lung metastasis of breast cancer.

To prepare the r9-CN nanovehicle, the r9 peptide was linked to 1,2-dioleoyl-sn-glycero-3-phospho-ethanolamine (DOPE) via disulfide bonds to form the conjugate r9-S-S-DOPE. CTX, a potent microtubule-disrupting agent, was selected as the anticancer drug for anti-metastasis therapy [40]. The r9-CN nanovehicles were assembled from r9-S-S-DOPE, 1,2-distearoyl-sn-glycero-3-phosphoethanolamine-N-methoxy-polyethylene glycol-2000 (DSPE-PEG2000) and the anticancer drug CTX. The cellular uptake of r9-CN and the associated therapeutic effects were measured in metastatic 4T1 cancer cells. In a lymphatic metastasis model, the specific targeting and deep penetration of r9-CN in primary tumor and regional lymphatic metastasis sites were delicately investigated after intravenous injection. The curative effects of r9-CN on primary tumor growth, lymphatic metastasis, and distant lung metastasis were evaluated to validate the feasibility of the proposed nanovehicle for anti-metastasis therapy.

Methods

Materials

DSPE-PEG2000 and DOPE were provided by Shanghai Advanced Vehicle Technology Pharmaceutical, Ltd. (Shanghai, China). The r9 peptide (Sequence: rrrrrrrrrc-SH) was synthesized by GL Bio-chem (Shanghai), Ltd. (Shanghai, China). The conjugate of r9-S-S-DOPE was synthesized following our previously described method [39]. CTX was provided by Shanghai Chemleader Biomedical Co., Ltd. (Shanghai, China). Sulforhodamine B was purchased from Sigma-Aldrich (Shanghai, China). 1′-dioctadecyl-3, 3, 3′, 3′-tetramethylindotricarbocyanine iodide (DiR) and DL-dithiothreitol (DTT) were obtained from Dalian Meilun Biotechnology Co., Ltd. (Dalian, China). Hoechst 33342, FITC-actin tracker, and 4′, 6-diamidino-2-phenylindole (DAPI) were purchased from Beyotime Institute of Biotechnology (Jiangsu, China).

Preparation and characterization of r9-CN

The r9-CN was fabricated from DSPE-PEG2000, r9-S-S-DOPE, and the anticancer drug CTX (8:1:1, w/w) by a self-assembly operation. Briefly, these components were dissolved in 4 mL of methanol and evaporated to form a lipid film in a round flask using a rotary evaporator. The film was then dispersed into phosphate buffered solution (PBS pH 7.4) to prepare the r9-CN. By contrast, a bare nanovehicle of CTX without r9-S-S-DOPE (CN) was prepared with DSPE-PEG2000 and CTX following the same procedure.

The particle size distribution and zeta potential of r9-CN and CN were measured by dynamic light scattering (DLS) using a Malvern Zetasizer Nano ZS 90 instrument (Malvern, UK). The morphology was imaged with a field emission transmission electron microscope (FE-TEM, FEI Tecnai G2 F20 S-Twin, USA). The encapsulation efficiency of CTX in these two micelles was analyzed by high-performance liquid chromatography (HPLC, Shimadzu, Japan) with a BEH X Bridge C_{18} column (4.6-mm diameter, 250-mm length, 5-μm thickness); an acetonitrile-water (70:30, v/v) mobile phase; a flow rate of 1 mL/min; and a detection wavelength of 230 nm. The un-encapsulated drug was separated from the micelles by centrifugation, and the drug amount was determined by HPLC. The CTX loading capacity in CN and r9-CN was also determined. These measurements were performed in triplicate.

To evaluate the stability of these two micelles in physiological solutions, samples were respectively mixed with PBS (pH 7.4) and PBS (pH 7.4) containing 10% fetal bovine serum (FBS). At certain time intervals, the encapsulation efficiency values were determined by the HPLC method as described above. The particle size distribution was analyzed by DLS.

Moreover, the in vitro release profiles of CTX from these two micelles were evaluated in PBS at different pH values of 7.4 and 4.7, and in PBS (pH 7.4) containing reductive DTT (10 mM). In brief, 100 μL of micelles were added to 900 μL of release media and incubated at 37 °C and 100 rpm. At predetermined time intervals, samples were collected and centrifuged to separate the released CTX. The drug amount was determined by the aforementioned HPLC procedure.

Cell uptake

The in vitro evaluations were measured in a metastatic 4T1 breast cancer cell line, which was obtained from Cell Bank of Shanghai, Chinese Academy of Sciences (Shanghai, China). Cells were cultured in RPMI-1640 media (Gibco, USA) supplemented with 10% FBS, 1% streptomycin, and 1% penicillin, and maintained in a humidified incubator at 37 °C with 5% CO_2 for further measurements.

The cellular uptake of r9-CN and CN was visualized with a laser confocal scanning microscope (LCSM, Leica TCS-SP8 STED, Germany). Micelles were fluorescently labeled with hydrophobic DiR probes by physical entrapment. The 4T1 cells were seeded into a 24-well plate at 4×10^4 cells/well and cultured overnight. The DiR-labeled r9-CN and CN were then added to each well with 10 μg/mL of DiR and incubated for 8 h. At 2.0, 4.0, and 8.0 h of incubation, the nuclei were stained with Hoechst 33342 (blue) and the lysosomes were counterstained

with LysoTracker Green DND-26 (green) for visualization under LCSM.

The cellular uptakes of r9-CN and CN were then quantified by HPLC as describe above. Briefly, 4T1 cells were seeded into a 6-well plate at 3×10^5 cells per well and cultured overnight. The r9-CN and CN micelles were added to each well at 50 μg/mL of CTX and incubated for 8 h. At 2.0, 4.0, and 8.0 h of incubation, cells were lysed using a cell lysis buffer (Meilun Bio, China) for 30 min at 37 °C. The lysates were collected, freeze-dried, dissolved with 200 μL of methanol, and centrifuged at 9000 rcf for 5 min. The drug amount in the supernatant was analyzed using the HPLC method as described above.

Cell cytotoxicity

The cytotoxicities of r9-CN and CN were measured in metastatic 4T1 cancer cells using sulforthodamine B assays (Sigma-Aldrich, USA). Cells were seeded into a 96-well plate at 3×10^3 cells per well and cultured overnight. Free CTX, CN, and r9-CN were then added to each well, with CTX concentrations ranging from 0.01 to 200 μg/mL, and incubated for an additional 50 h. The cell viabilities in each group were determined using sulforthodamine B (Enspire, Perkin-Elmer, Singapore). Cells without any treatment were performed as negative control.

Inhibitory effects on cell migration

The inhibitory effects of r9-CN on the migration activity of metastatic 4T1 cells were measured by a transwell-mediated cell migration assay. Briefly, 200 μL of FBS-free RPMI1640 media with 2×10^5 4T1 cells were seeded into the upper chambers of inserts (24-well, pore size: 8 μm; Costar, USA), and 600 μL of culture media with 10% FBS were added to the lower plates as the chemo-attractant to induce cell migration. Various samples of r9-CN, CN, free CTX, and blank r9-N micelles were then added to the upper and lower chambers at 400 ng/mL of CTX or an equivalent dose. After 24 h, the migrated cells were stained with crystal violet solution and imaged under a microscope (Olympus IX81, Japan). Cells without any treatment were imaged as a negative control. The inhibitory effects on cell migration were defined as the ratio between the migrated cells in each group compared to that in the negative control.

Animals and lymph metastatic model

Female nude mice (4- to 6-weeks-old) were provided by the Shanghai Laboratory Animal Center, Chinese Academy of Sciences. The in vivo experiments were performed under guidelines approved the Institutional Animal Care and Use Committee of Shanghai Institute of Materia Medica, Chinese Academy of Sciences. After 3-5 days of acclimatization, 4T1 cells were injected into the right hind footpad, with 5×10^5 cells in 25 μL of FBS-free RPMI-1640 media per mouse to develop the lymph metastatic breast cancer model.

In vivo specific targeting to primary tumor and lymph metastasis

The DiR-labeled micelles of CN and r9-CN were used for the in vivo measurements. When the volume of 4T1 tumors reached 300–400 mm^3 with obviously swollen lymph nodes, the nude mice were administered with free DiR, CN, and r9-CN at 2 mg/kg DiR via tail vein injection. At predetermined time intervals, the mice were anesthetized and the DiR fluorescence signals were recorded by an in vivo imaging system (IVIS Spectrum, Perkin-Elmer, USA) (ex: 745 nm; filters: 780 nm). At 2.0, 8.0, and 24 h after drug administration, mice were euthanized, and the cardinal organs (including heart, liver, spleen, lung, and kidneys); primary tumor, and nearby metastatic lymph node were carefully collected and imaged with the in vivo imaging system. The intensities of fluorescence signals from each organ were recorded for further quantification.

The deep penetration of r9-CN in the primary tumor and lymphatic metastasis were then visualized by LCSM (Leica TCS-SP8 STED, Germany). The tumor mass and the lymph node were collected, frozen in cryo-embedding media and sectioned (CM1950, Leica, Germany) at 10 μm for further measurements. The sections were stained with DAPI (blue) and Actin Tracker Green for visualization under LCSM. The images were recorded using the Leica Application Suite X (LAS X) software. The micelles were depicted as red signals in the acquired images.

In vivo therapeutic efficacy against primary tumor growth, lymph node metastasis, and distant lung metastasis

The therapeutic effects of r9-CN were measured in a lymphatic metastasis model. When the tumor size reached approximately 100 mm^3, four mice were randomly assigned to each of five groups and respectively treated every three days with a PBS control, blank r9-N micelles, free CTX, CN, or r9-CN at 10 mg/kg or an equivalent dose. The body weights of the mice and the lengths and widths of their primary tumor tissues were detected at certain time intervals. At day 23 after the treatment, mice were autopsied and the tumor mass, lymph node near the primary tumor, and lung tissues were collected. The tumor mass and lymph node were weighed to calculate the inhibitory rate against tumor growth and lymph metastasis. The visualized metastatic nodules in lungs from each group were counted to evaluate

their inhibition of distant metastasis. Moreover, the lung tissues from each group were histologically examined by Hematoxylin and Eosin staining kit.

Statistical analysis

Data are presented as mean ± standard deviation. A two-tailed student's t-test was used to detect the statistical difference in a two-group comparison, and the difference was regarded as significant when the p value was less than 0.05.

Results and discussion

Preparation and characterization of r9-CN

The r9-CN micelle system was fabricated from DSPE-PEG, r9-S-S-DOPE and CTX by self-assembly, whereas the CN micelle system constituted only DSPE-PEG2000 and CTX. The r9-S-S-DOPE conjugate was synthesized by linking the cell-penetrating peptide and the phospholipid DOPE to form an amphiphilic conjugate, which was used in combination with amphiphilic lipids of DSPE-PEG2000 to fabricate the cell-penetrating peptide-based nanoassembly of r9-CN. The DLS analysis indicated that both CN and r9-CN were nanometer-sized particles with mean diameters of 14.67±4.21 nm and 13.22±3.47 nm, respectively (**Figure 2A**). The FE-TEM images showed that both CN and r9-CN consisted of homogeneous spherical nanoassemblies (**Figure 2B**). These results suggested that the incorporation of r9 peptide in r9-CN did not impact the particle size of the micelles system. Moreover, the DLS measurements showed that the zeta potential value was –2.45±0.76 mV for CN, changing slightly to 0.75±1.48 mV for r9-CN. In addition, the HPLC results indicated that the CTX encapsulation efficiency was 96.86±0.01% in r9-CN and 96.35±0.04% in CN. The CTX loading capacity was 4.45±0.05% for CN and 3.45±0.01% for r9-CN. When they were mixed with PBS (pH 7.4) or PBS (pH 7.4) with 10% FBS, the CTX encapsulation efficiency values in CN and r9-CN, as well as their mean diameters, were not statistically changed within 24 h, indicating their good stability in the mimicked physiological fluids (**Figure 2C**).

The CTX release profiles from CN and r9-CN were determined in PBS at different pH values or in PBS with 10 mM DTT (**Figure 2D-E**). The cumulative drug release from CN and r9-CN within 8 h was less than 10% in PBS at pH 7.4 and 4.7. Moreover, in PBS with 10 mM of DTT, the cumulative drug release within 8 h from r9-CN was over 20%, which was much higher than that from CN. The increased drug release from r9-CN compared to CN could be due to the incorporation of r9-S-S-DOPE in the r9-CN system. These results suggested that the r9-CN exhibited a reduction-sensitive drug release, which could have beneficial antitumor effects. In addition, the limited drug release from these two micelles in PBS at pH 7.4 also verified their good stability over time. Compelling evidence has indicated that smaller nanovehicles (particularly sub-30 nm) are preferred for enhanced tumor penetration and lymph node targeting [11, 24, 41, 42]. In vitro evaluations have suggested that neutral nanoparticles (±10 mV) could be transported across an extracellular matrix faster and over greater distances than charged analogs [43, 44]. Moreover, a recent study showed that polymeric nanoparticles with slight positive surface charges (+3.5 mV) achieved better tumor accumulation and deep penetration [45]. In this work, r9-CN exhibited a near neutral zeta potential (+0.75 mV) and small particle size (13 nm), thereby exhibiting great promise for effective lymph metastases targeting and deep penetration in tumor masses.

In vitro cellular uptake and therapeutic effects

At different time intervals during incubation, the red DiR fluorescence signals were extensively visualized with strong intensity in r9-CN-treated 4T1 cells (**Figure 3A**), indicating the efficient cellular internalization by the cell-penetrating peptide-based r9-CN nanovehicle. Moreover, the cellular uptake of r9-CN and CN in 4T1 cells was quantified by measuring the CTX concentrations. The HPLC results indicated that the CTX concentrations from 4T1 cells treated with r9-CN were respectively 1.60-, 1.73- and 1.78-fold higher than those of CN at 2 h, 4 h, and 8 h of incubation (**Figure 3B**). The extensively enhanced cellular uptake of r9-CN over CN could be mainly ascribed to the incorporation of the r9 cell-penetrating peptide in the r9-CN micelle system. Moreover, with the extension of the incubation time to 8 h, many red signals were detected in the cytoplasm (**Figure 3A**), suggesting efficient intracellular drug delivery by r9-CN. Because CTX is a potent anticancer drug that works against microtubules in the cytoplasm [46], the efficient intracellular delivery achieved with r9-CN could be favorable for therapeutic effects. The increased intracellular delivery of r9-CN over CN could be attributed to the ability of the r9-S-S-DOPE conjugates to escape endosomes.

In view of the efficient cell uptake of r9-CN in 4T1 cells, the nanovehicle's inhibitory effects on cancer cell viability were determined. As shown in **Figure 3C**, free CTX, CN, and r9-CN showed significant inhibition of the viability of metastatic 4T1 cancer cells in a concentration-dependent manner (**Figure 3C**). Compared to the free CTX group, the average half-maximal inhibitory concentration (IC_{50}) value of r9-CN (0.03 μg/mL) was remarkably reduced

by 223-fold, whereas that of CN was only slightly less than that of the free CTX. In addition, the IC_{50} value of r9-CN was drastically decreased by 165-fold compared to that of CN. Therefore, r9-CN prominently enhanced cytotoxicity in 4T1 cells compared to CN, which could be mainly ascribed to the incorporation of r9-S-S-DOPE in the r9-CN system.

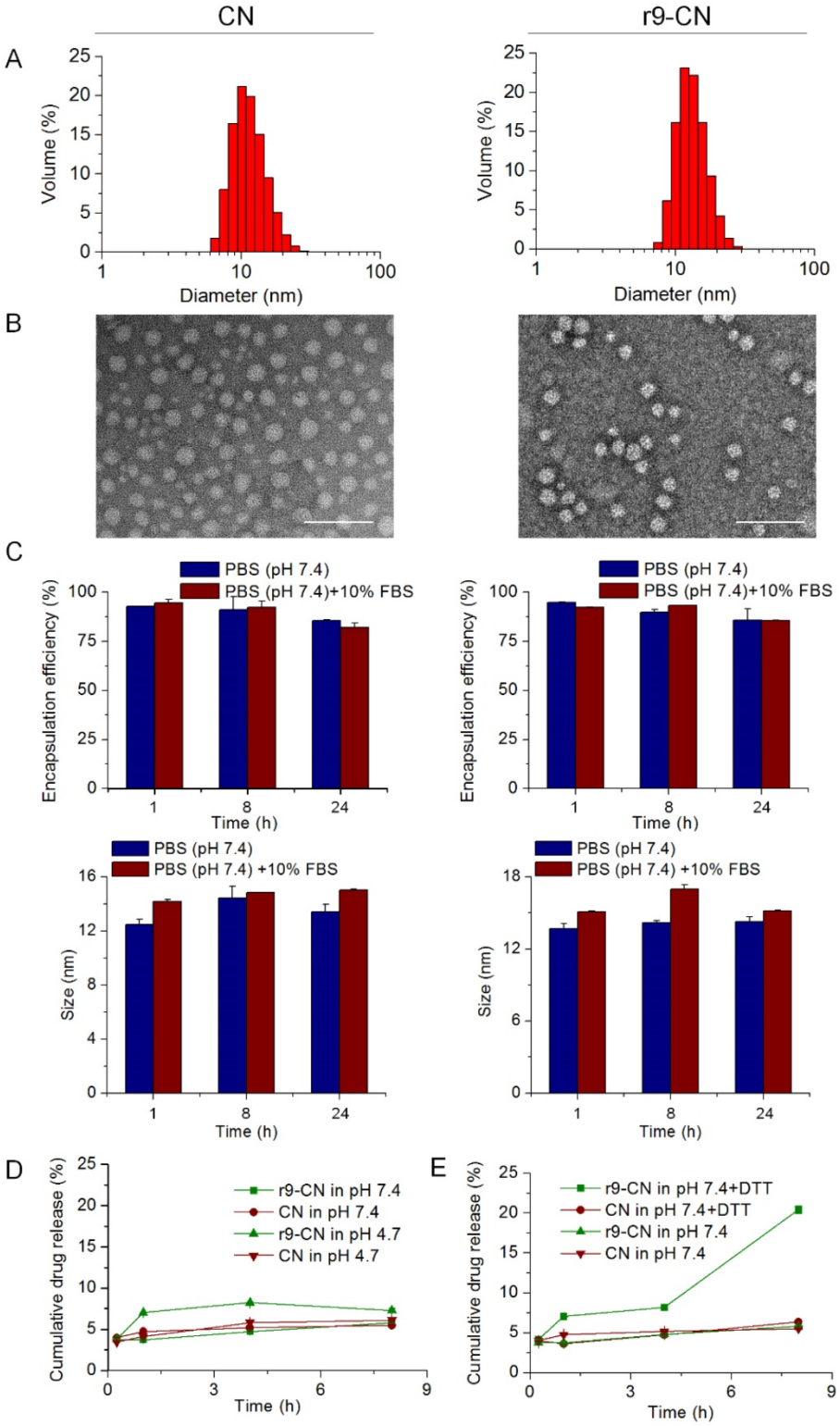

Figure 2. Characterizations of r9-CN and CN. (A) Size distribution of CN and r9-CN measured by DLS. **(B)** Typical FE-TEM images; scale bar = 100 nm. **(C)** Stability of CN and R9-CN in PBS (pH 7.4) or PBS (pH 7.4) with 10% FBS over time, characterized by the CTX encapsulation efficiency in the nanovehicles and the particle size at certain time intervals within 24 h. **(D)** In vitro release profiles of CN and r9-CN in PBS at pH 7.4 and 4.7. **(E)** In vitro release profiles of CN and r9-CN in PBS with and without reductive DTT.

The anti-migration activities of r9-CN and CN were measured using a transwell-mediated assay. Compared to the negative control, the blank r9 micelles without CTX (r9-N) showed slight inhibition of the cell migration activity (**Figure 3D-E**). However, in the free CTX group, the number of cells migrating across the transwell membrane was significantly decreased to 22.65% of the number that migrated with the negative control, and the number was drastically reduced by 96.33% in the CN group. In the r9-CN group, the number of cells that migrated across the transwell membrane was almost negligible, suggesting the exceeding inhibitory effects of r9-CN on cell migration. Therefore, the migration activity of metastatic 4T1 cells could be notably suppressed by r9-CN and CN, offering great promise for in vivo anti-metastasis therapy.

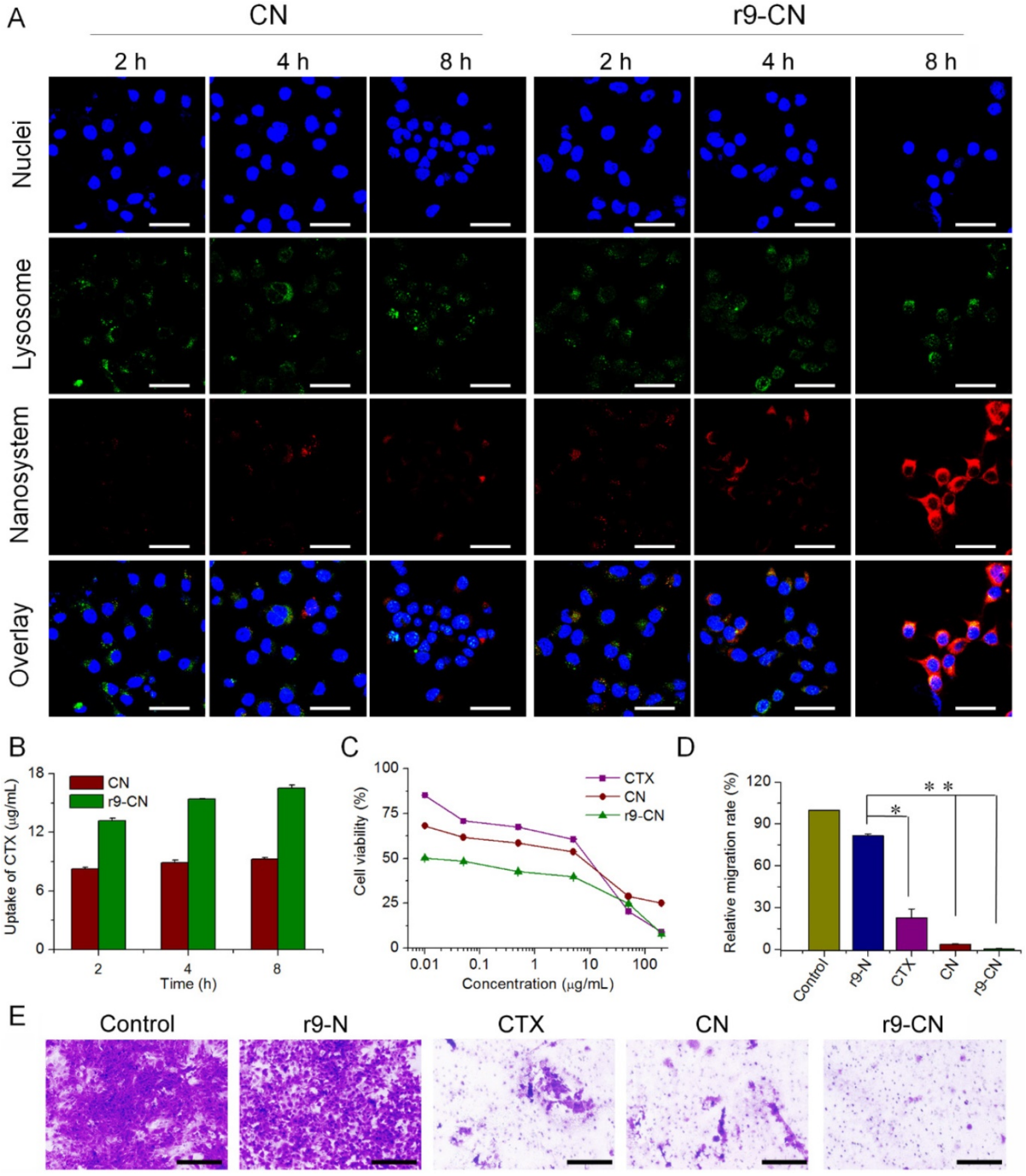

Figure 3. Cellular uptake and in vitro therapeutic effects of r9-CN and CN in metastatic 4T1 cells. (A) Cellular uptake in 4T1 cells under LCSM; scale bar = 40 μm. **(B)** Quantified cellular internalization in 4T1 cells determined by flow cytometry; *p < 0.05. **(C)** Cytotoxicity of CTX, CN, and r9-CN in metastatic 4T1 cells. **(D)** Percentage of cells migrating across the transwell membrane compared to the negative control; *p < 0.05, **p < 0.01. **(E)** Typical images of cell migration across the transwell membrane, where cell clusters are illustrated as violet regions; scale bar = 200 μm.

In vivo specific targeting and deep penetration in lymph metastases

The specific targeting of r9-CN to a primary tumor and lymphatic metastases was evaluated in a lymph metastatic breast cancer model. As exhibited in **Figure 4A**, the fluorescence signals could be clearly detected from the original tumor locations and from nearby metastatic lymph glands in the r9-CN and CN groups, and the signal intensities were gradually enhanced with time up to 8 h, leveling off thereafter for the remaining 24 h (**Figure 4A**). At 2, 8, and 24 h after the injections, the major organs as well as the original tumor tissues and metastatic lymphatic glands were collected for imaging. The fluorescence signals could be mainly detected from the liver, tumor, and lymph nodes, indicating the efficient targeting ability of r9-CN and CN to the primary tumor and metastatic lymph nodes (**Figure 4B**). In primary tumor sites, the fluorescence signals from the r9-CN and CN groups were maintained at a high level even at 24 h post-injection, whereas the signals from free DiR were rapidly eliminated with the extension of time.

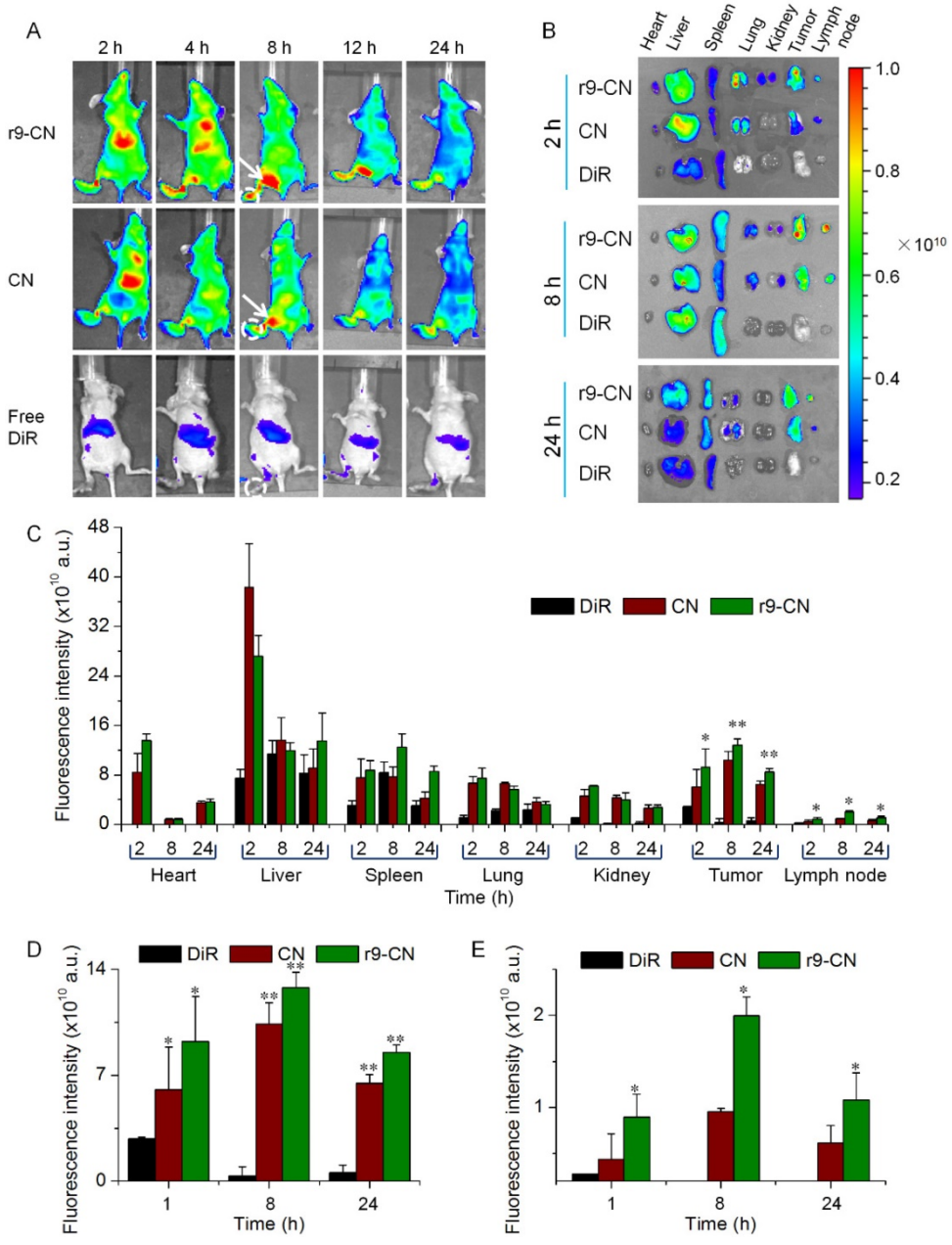

Figure 4. In vivo specific targeting of CN and r9-CN to primary tumor and metastatic lymph nodes at different time intervals. (A) In vivo imaging of DiR-labeled r9-CN and CN in a lymph metastatic breast cancer model: white circles are the primary tumor sites in foot pads; white arrows are metastatic lymph node sites. **(B)** Ex vivo distribution of DiR-labeled r9-CN and CN in major organs. **(C)** Quantified distribution of DiR-labeled r9-CN and CN in major organs from each group. **(D)** Quantified distribution of DiR-labeled r9-CN and CN in primary tumor. **(E)** Quantified distribution of DiR-labeled r9-CN and CN in metastatic lymph nodes; *p < 0.05, **p < 0.01.

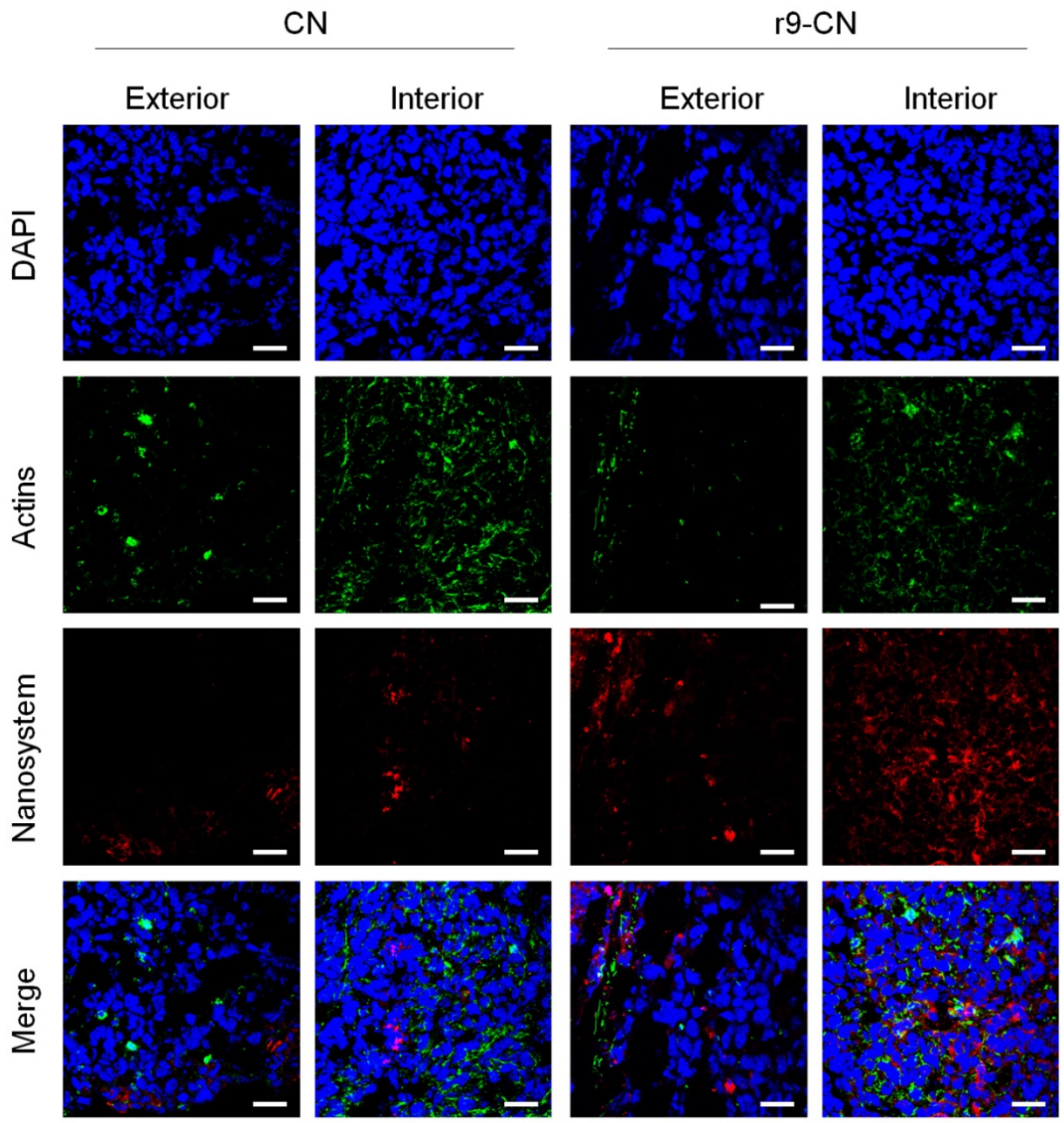

Figure 5. In vivo tumor penetration and cellular internalization of r9-CN in exterior and interior regions of primary tumor at 8.0 h of injection. Sections were stained with DAPI and Actin-tracker for visualization under LCSM; scale bar = 25 μm.

Compared to that of the free DiR group, the fluorescence intensities of CN and r9-CN in tumors at 8 h post-injection were notably enhanced by 30.2- and 37.2-fold, respectively (**Figure 4C-D**). These results revealed that r9-CN and CN could be efficiently accumulated in tumor sites with long retention times, demonstrating great potential for effective anti-tumor therapy. In metastatic lymph nodes, the fluorescence intensities from the r9-CN group were significantly increased by 2.06-, 2.09-, and 1.73-fold compared to CN at 2, 8, and 24 h after injection, indicating effective in vivo lymph metastasis targeting via intravenous injection (**Figure 4C, E**). By comparing the components of r9-CN and CN, the r9 cell-penetrating peptide in r9-CN was considered to account for the significant enhancement of primary tumor and lymph metastasis targeting. In addition, nanovehicles within 6–34 nm are preferred for lymph node targeting [11]. The small particle size of the r9-CN system could also satisfy this essential prerequisite for the efficient targeting of original tumor and regional lymphatic metastases.

The limited penetration of nanovehicles in tumor or metastases has been evidenced as a major factor limiting their therapeutic efficacy [47-49]. The lymph nodes near the original tumor are often the most susceptible sites of metastasis [8, 50, 51]. Therefore, the extent of tumor penetration and cellular internalization of r9-CN in primary tumor and metastatic lymph nodes were respectively evaluated. In the primary tumor (**Figure 5**), the red fluorescence signals from the CN group could be detected in the exterior regions of the tumor mass with strong intensity but were only weakly observed in the deep interior, indicating the restricted penetration of CN in the primary tumor. By contrast, the signals from the

r9-CN group could be extensively visualized in both the exterior and interior regions of the primary tumor with strong intensity, suggesting enhanced tumor penetration. Moreover, the r9-CN could be largely internalized by cancer cells, offering great promise for therapeutic effects.

Likewise, in all of the images of the metastatic lymph nodes (**Figure 6**), the red signals from the CN group were mainly observed in the outer area of the lymph nodes, and the intensity was exponentially reduced upon their direction to the center of metastatic lymph nodes, indicating the limited transport of CN into the deep interior and poor accessibility to cancer cells (**Figure 6A-B**). Conversely, in the r9-CN group, the red fluorescence could be clearly detected with high intensity throughout the whole metastatic lymph node, validating r9-CN's efficient penetration ability (**Figure 6C**). In typical images of exterior and interior regions, r9-CN could be readily visualized in cancer cells at the metastatic lymph nodes (**Figure 6D**), indicating their massive uptake by cancer cells in lymph metastasis. These results confirmed the extensive penetration and efficient cellular internalization of r9-CN in tumor masses and metastatic lymph nodes, a considerable improvement over the corresponding CN results. When compared to the CN components, the increased tumor penetration and cellular accessibility of r9-CN in metastatic lymph nodes could be mainly ascribed to the incorporation of the r9 cell-penetrating peptide and its appropriate combination with DSPE-PEG2000 in the r9-CN system.

The efficient transport of r9-CN into metastatic lymph nodes after intravenous injection could be owing to the small particle size (13 nm), neutral surface charge (+0.75 mV), and outstanding penetrating effects of the r9 peptide in the r9-CN system. Kataoka and co-workers performed real-time micro-distribution assays in metastatic lymph nodes and found that the small-sized micelles exhibited higher selectivity for metastasis in lymph nodes. The intravenously-administered 30-nm micelles could extravasate from the blood vasculature in metastases and penetrate the metastatic mass [24]. Moreover, in vitro evaluations have suggested that the neutral surface charge of nanoparticles would facilitate their diffusion across the extracellular matrix [43, 44]. In particular, the D-enantiomers analog of the r9 peptide have shown a prominent ability to promote their accumulation in tumor tissues [37]. The synergistic

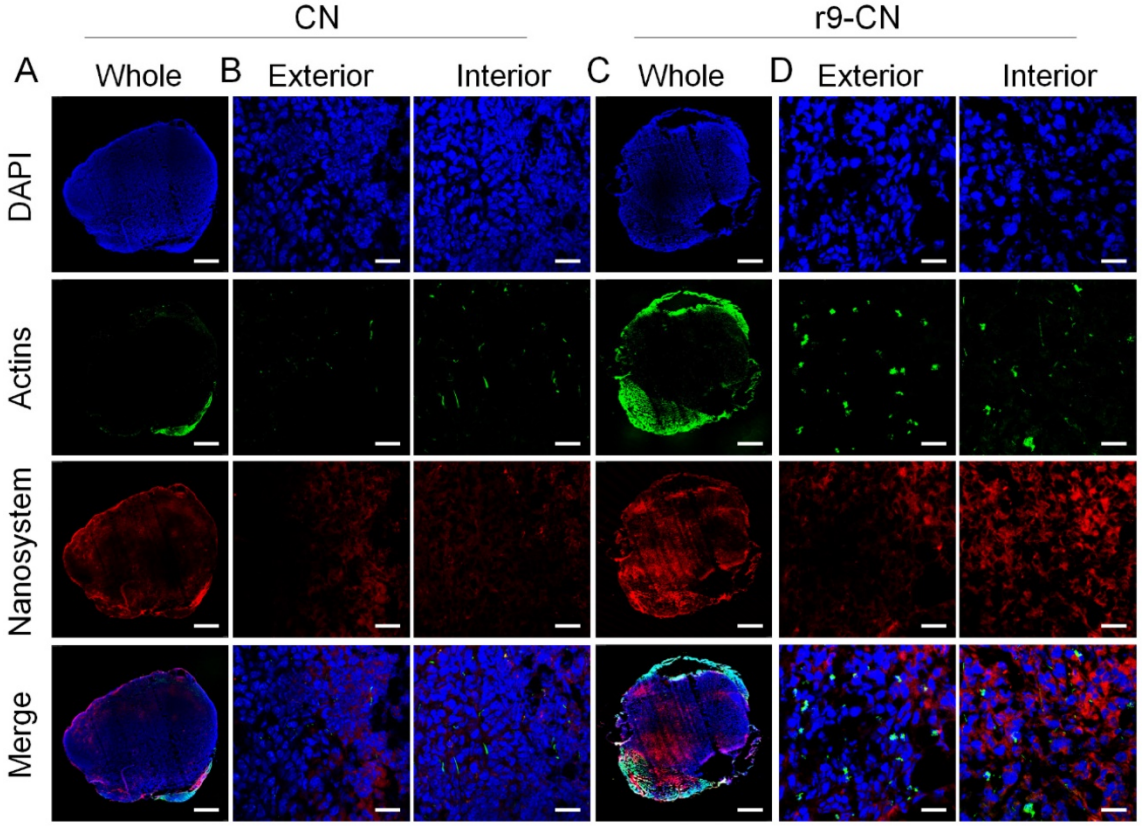

Figure 6. In vivo specific targeting, deep penetration, and cellular internalization of r9-CN in metastatic lymph nodes, detected under LCSM at 8.0 h after injection. The nuclei (blue) and F-actin (green) were respectively stained for the visualization. **(A)** Whole image of metastatic lymph after intravenous injection of DiR-loaded CN; scale bar = 500 μm. **(B)** Enlarged images of the uptake of CN in the exterior and interior regions of metastatic lymph nodes; scale bar = 25 μm. **(C)** Whole image of metastatic lymph after intravenous injection of DiR-loaded r9-CN; scale bar = 500 μm. **(D)** Enlarged images of the uptake of r9-CN in the exterior and interior regions of metastatic lymph nodes; scale bar = 25 μm.

combination of these factors in r9-CN would be expected to facilitate their specific accumulation in primary tumors, diffusion across extracellular matrix barriers, and deep penetration into tumor masses. During the initial metastasis of cancer cells from a primary tumor, the lymphatic vessels around the primary tumor undergo dynamic changes, including lymph angiogenesis and lymphatic enlargement, to increase the spread of tumor cells to distant sites [8]. In this manner, r9-CN would be allowed to diffuse across the interstitial environments into the remodeled lymphatic vessels to facilitate their efficient targeting to the lymph metastasis, wherein r9-CN's small particle size and other advantageous effects of the r9 peptide would play a key role in their efficient lymph metastasis targeting and deep penetration.

In vivo therapeutic efficacy against tumor growth, regional lymph metastasis, and distant lung metastasis

The in vivo curative effects of r9-CN on tumor growth and metastasis were determined in a model of lymphatic metastasis of breast cancer. The inhibitory effects of r9-CN on primary tumor progression, regional lymph node metastasis, and distant lung metastasis were investigated. In the primary tumor growth profiles (**Figure 7A**), the tumor size under treatment with blank r9-N rapidly increased with time, indicating failure to inhibit tumor growth. By contrast, the tumor growths were moderately suppressed by 47.7% in the free CTX group and 52.6% in the CN group.

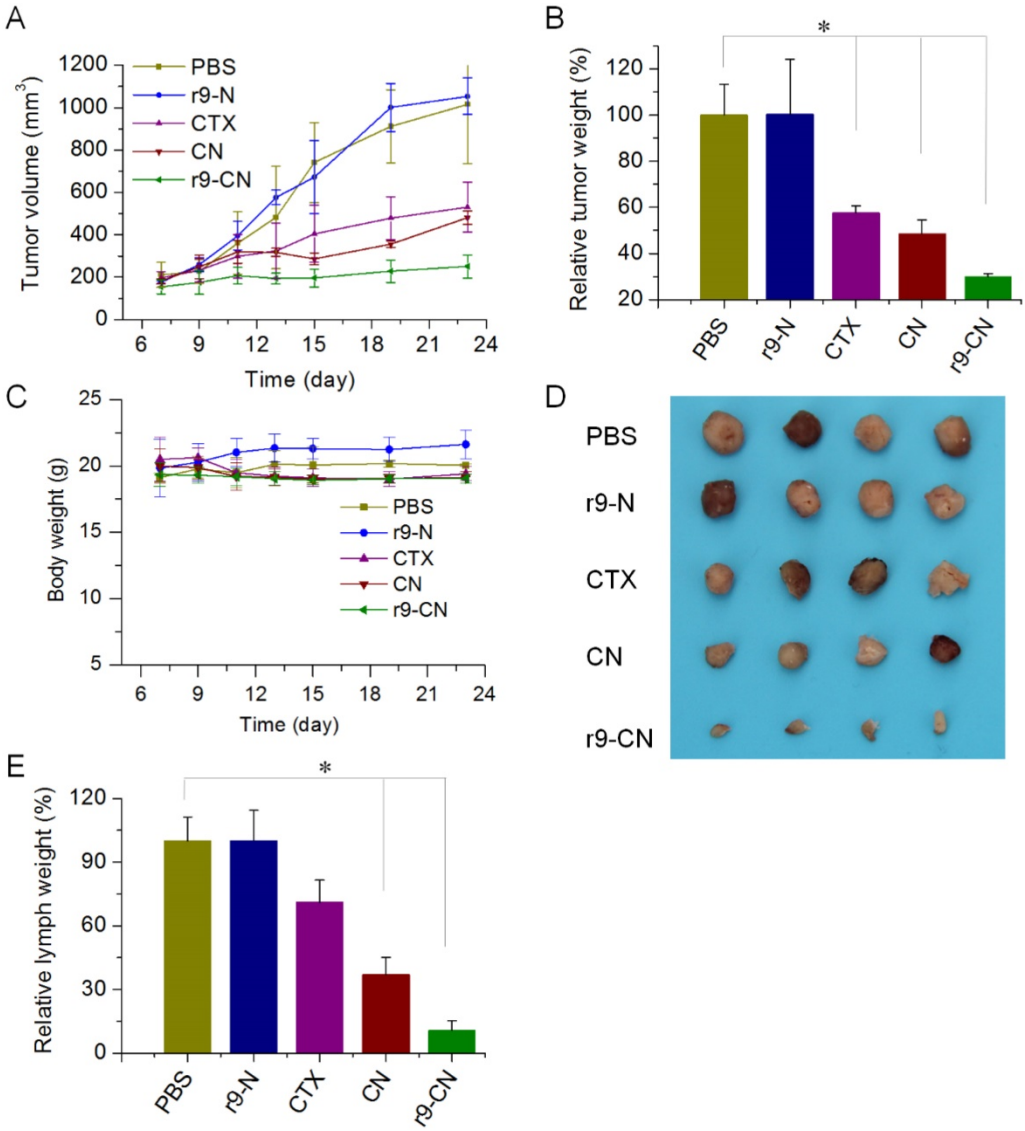

Figure 7. Therapeutic effects of r9-CN against primary tumor progression and lymphatic metastasis of breast cancer. (A) Tumor growth profiles of primary tumor from each group. **(B)** Inhibition of primary tumor growth by various formulations; *p < 0.05. **(C)** Body weight changes in mice from each group. **(D)** Typical images of metastatic lymph nodes from different treatments. **(E)** Inhibition of the metastatic lymph nodes by various formulations; *p < 0.05.

However, in the r9-CN-treated group, the tumor growth was clearly suppressed with an inhibition rate of 75.3%, which was 1.6-fold and 1.4-fold higher than the suppression induced by free CTX and CN, respectively. We also measured the weight of the tumor mass from each group and confirmed that r9-CN had the most efficient inhibitory effects on primary tumor growth (**Figure 7B**). In addition, the body weights of the mice from each group were not significantly changed during these treatments, indicating the favorable biosafety of the CN and r9-CN systems (**Figure 7C**).

At the early stage of metastasis, cancer cells usually spread through the lymphatic vessels and reach nearby regional lymph nodes. Swollen lymph nodes with increased size and weight was found to be a credible index of lymph metastasis in previous reports [8, 24]. We collected and imaged the swollen lymph nodes near the primary tumor (**Figure 7D**) and measured their weight to quantify the inhibition rates of lymph node metastasis. As shown in **Figure 7E**, the free CTX showed slight inhibition of lymph node metastasis and blank r9-N had no inhibitory effects. By contrast, the CN treatment presented a moderate inhibition rate of 63.1% compared to the negative control. In the r9-CN group, the average lymph node weight was markedly reduced to only 10.9% that of the negative control, an 89.1% inhibition of lymph node metastasis. Moreover, the lymph node weight in mice treated with r9-CN was only 15.3% and 29.5% of the corresponding values in mice treated with free CTX and CN, respectively. When compared to free CTX and CN, the inhibitory effects of r9-CN were significantly improved by 3.1-fold and 1.4-fold, respectively, confirming the superior therapeutic effects of r9-CN on inhibiting regional lymph node metastasis associated with breast cancer.

Moreover, in the advanced stage of cancer metastasis, the lung tissues are among the most frequent sites of cancer cell spread, and metastasis to these tissues usually causes the death of breast cancer patients [4, 52, 53]. After the final time interval, the lung tissues were collected, and the visualized metastatic nodules in each lung were calculated to evaluate the inhibitory effects on lung metastasis (**Figure 8A**). In the saline control and blank r9-N group, metastatic nodules were largely detected in lungs, suggesting the extensive incidence of lung metastasis. When mice were treated with free CTX, the incidence of lung metastasis was moderately reduced to 30.7% that of the negative control, and the CN group showed a significant reduction of 90.9%. In the r9-CN treated group (**Figure 8B**), the average number of lung metastatic nodules was only 0.75±1, which was only 3.4%, 11.1%, and 37.5% of the corresponding values from the negative control, free CTX, and CN groups, respectively. Therefore, the r9-CN treatment produced a 96.6% inhibition of lung metastasis, which was much more effective than both free CTX and CN. Moreover, we further performed histological examinations of lung tissues from each

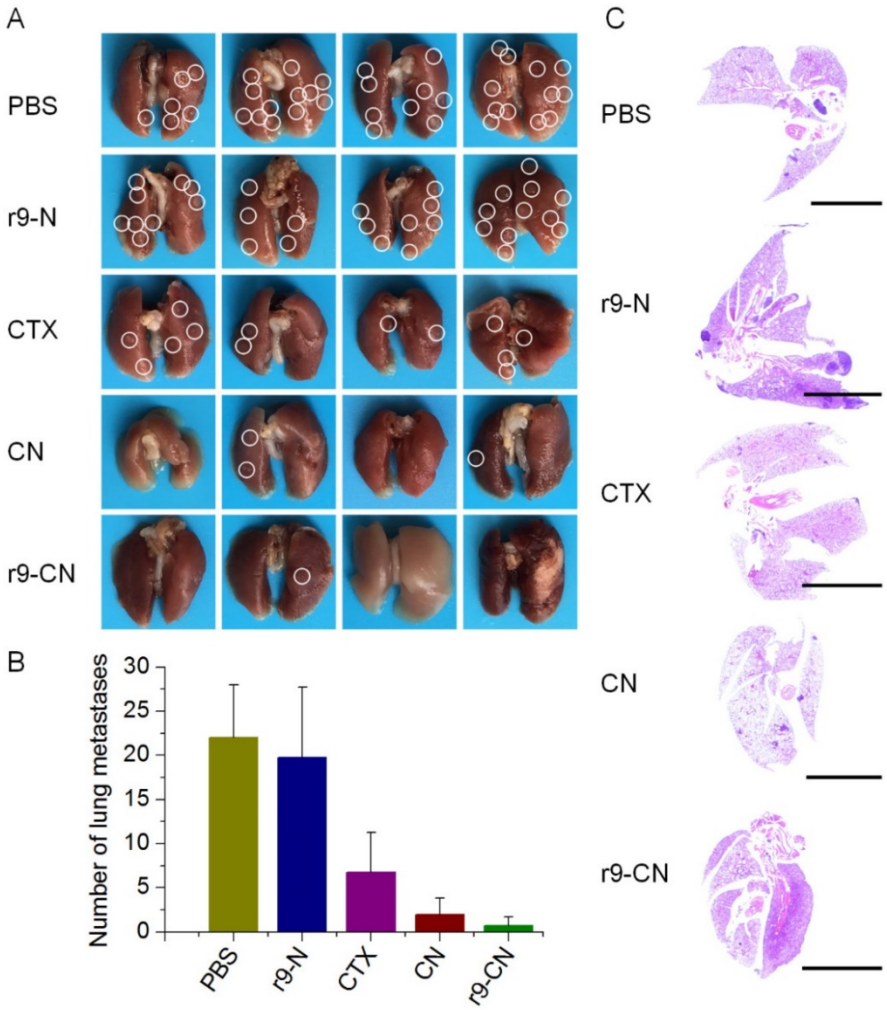

Figure 8. In vivo therapeutic effects of r9-CN on inhibiting distant lung metastasis of breast cancer. (A) Typical images of lung tissues from PBS, blank r9-N, CTX, CN, and r9-CN groups; white circles denote visually-detected metastatic nodules in the lung. **(B)** Average number of metastatic nodules in lungs from various formulations; *p < 0.05, **p < 0.01. **(C)** Histological examinations of whole lung tissues by Hematoxylin and Eosin staining from each group; scale bar = 5000 μm.

group and confirmed the superior inhibitory effects of r9-CN on the incidence of lung metastasis (**Figure 8C**). In view of the significant enhancement of r9-CN over CN for tumor penetration and cellular internalization, the r9 cell-penetrating peptide in r9-CN was considered to play a substantial role in the improved therapeutic outcomes for tumor growth and metastasis.

Conclusion

In summary, we successfully developed a r9-CN nanoplatform with efficient lymph metastasis targeting and deep penetration ability for effective anti-metastasis therapy. The r9-CN was a homogeneous nanometer-sized particle with a mean diameter of 13 nm and neutral surface charge. In the lymphatic metastatic model, r9-CN was preferentially delivered to the primary tumor sites and nearby metastatic lymph nodes, and then infiltrated both the exterior and interior of the tumor mass. Moreover, the r9-CN treatment produced remarkable inhibition of primary tumor growth, regional lymph nodes metastasis, and distant lung metastasis. Therefore, the r9-CN system could provide an effective drug delivery platform with efficient lymph metastasis targeting and favorable penetration capacity to improve therapeutic outcomes against cancer metastasis.

Abbreviations

CTX: cabazitaxel; DAPI: 4′, 6-diamidino-2-phenylindole; DiR: 1, 1′-dioctadecyl-3, 3, 3′, 3′-tetramethylindotricarbocyanine Iodide; DLS: dynamic light scattering; DOPE: 1, 2-dioleoyl-sn-glycero-3-phosphorethanolamine; DSPE-PEG2000: 1, 2-distearoyl-sn-glycero-3-phosphoethanolamine-N-methoxy-polyethylene glycol-2000; DTT: DL-dithiothreitol; FBS: fetal bovine serum; HPLC: high-performance liquid chromatography; LCSM: laser confocal scanning microscope; PEG: polyethylene glycol; r9: D-oligoarginine peptide.

Acknowledgements

This work was supported by the National Basic Research Program of China (2015CB932103), the National Natural Science Foundation of China (31771092, 81521005, 81690265) and the Youth Innovation Promotion Association of the Chinese Academy of Sciences.

Competing Interests

The authors have declared that no competing interest exists.

References

[1] Miller KD, Siegel RL, Lin CC, Mariotto AB, Kramer JL, Rowland JH, et al. Cancer treatment and survivorship statistics, 2016. CA Cancer J Clin. 2016; 66: 271-89.
[2] Steeg PS. Targeting metastasis. Nat Rev Cancer. 2016; 16: 201-18.
[3] Nguyen DX, Bos PD, Massague J. Metastasis: from dissemination to organ-specific colonization. Nat Rev Cancer. 2009; 9: 274-84.
[4] Quail DF, Joyce JA. Microenvironmental regulation of tumor progression and metastasis. Nat Med. 2013; 19: 1423-37.
[5] Naxerova K, Reiter JG, Brachtel E, Lennerz JK, van de Wetering M, Rowan A, et al. Origins of lymphatic and distant metastases in human colorectal cancer. Science. 2017; 357: 55-60.
[6] Liu J, Meisner D, Kwong E, Wu XY, Johnston MR. Translymphatic chemotherapy by intrapleural placement of gelatin sponge containing biodegradable Paclitaxel colloids controls lymphatic metastasis in lung cancer. Cancer Res. 2009; 69: 1174-81.
[7] Ashitate Y, Hyun H, Kim SH, Lee JH, Henary M, Frangioni JV, et al. Simultaneous mapping of pan and sentinel lymph nodes for real-time image-guided surgery. Theranostics. 2014; 4: 693-700.
[8] Stacker SA, Williams SP, Karnezis T, Shayan R, Fox SB, Achen MG. Lymphangiogenesis and lymphatic vessel remodelling in cancer. Nat Rev Cancer. 2014; 14: 159-72.
[9] Cho JK, Hyun SH, Choi N, Kim MJ, Padera TP, Choi JY, et al. Significance of lymph node metastasis in cancer dissemination of head and neck cancer. Transl Oncol. 2015; 8: 119-25.
[10] Landesman-Milo D, Ramishetti S, Peer D. Nanomedicine as an emerging platform for metastatic lung cancer therapy. Cancer Metast Rev. 2015; 34: 291-301.
[11] Schroeder A, Heller DA, Winslow MM, Dahlman JE, Pratt GW, Langer R, et al. Treating metastatic cancer with nanotechnology. Nat Rev Cancer. 2011; 12: 39-50.
[12] Tammela T, Saaristo A, Holopainen T, Yla-Herttuala S, Andersson LC, Virolainen S, et al. Photodynamic ablation of lymphatic vessels and intralymphatic cancer cells prevents metastasis. Sci Transl Med. 2011; 3: 69ra11.
[13] Yi X, Yang K, Liang C, Zhong X, Ning P, Song G, et al. Imaging-guided combined photothermal and radiotherapy to treat subcutaneous and metastatic tumors using iodine-131-doped copper sulfide nanoparticles. Adv Funct Mater. 2015; 25: 4689-99.
[14] Liang C, Diao S, Wang C, Gong H, Liu T, Hong G, et al. Tumor metastasis inhibition by imaging-guided photothermal therapy with single-walled carbon nanotubes. Adv Mater. 2014; 26: 5646-52.
[15] Chen Q, Liang C, Wang X, He J, Li Y, Liu Z. An albumin-based theranostic nano-agent for dual-modal imaging guided photothermal therapy to inhibit lymphatic metastasis of cancer post surgery. Biomaterials. 2014; 35: 9355-62.
[16] Liang C, Song X, Chen Q, Liu T, Song G, Peng R, et al. Magnetic field-enhanced photothermal ablation of tumor sentinel lymph nodes to inhibit cancer metastasis. Small. 2015; 11: 4856-63.
[17] Zou L, Wang H, He B, Zeng L, Tan T, Cao H, et al. Current approaches of photothermal therapy in treating cancer metastasis with nanotherapeutics. Theranostics. 2016; 6: 762-72.
[18] Oussoren C, Storm G. Liposomes to target the lymphatics by subcutaneous administration. Adv Drug Deliv Rev. 2001; 50: 143-56.
[19] Ryan GM, Kaminskas LM, Porter CJ. Nano-chemotherapeutics: maximising lymphatic drug exposure to improve the treatment of lymph-metastatic cancers. J Control Release. 2014; 193: 241-56.
[20] Kikuchi S, Kishimoto H, Tazawa H, Hashimoto Y, Kuroda S, Nishizaki M, et al. Biological ablation of sentinel lymph node metastasis in submucosally invaded early gastrointestinal cancer. Mol Ther. 2015; 23: 501-9.
[21] Wang C, Xu L, Liang C, Xiang J, Peng R, Liu Z. Immunological responses triggered by photothermal therapy with carbon nanotubes in combination with anti-CTLA-4 therapy to inhibit cancer metastasis. Adv Mater. 2014; 26: 8154-62.
[22] Cao Y. Opinion: emerging mechanisms of tumour lymphangiogenesis and lymphatic metastasis. Nat Rev Cancer. 2005; 5: 735-43.
[23] Rafi M, Cabral H, Kano MR, Mi P, Iwata C, Yashiro M, et al. Polymeric micelles incorporating (1, 2-diaminocyclohexane)platinum (II) suppress the growth of orthotopic scirrhous gastric tumors and their lymph node metastasis. J Control Release. 2012; 159: 189-96.
[24] Cabral H, Makino J, Matsumoto Y, Mi P, Wu HL, Nomoto T, et al. Systemic targeting of lymph node metastasis through the blood vascular system by using size-controlled nano carriers. ACS Nano. 2015; 9: 4957-67.
[25] Carlson GW, Wood WC. Management of axillary lymph node metastasis in breast cancer: making progress. JAMA. 2011; 305: 606-7.
[26] Betticher DC, Schmitz SFH, Totsch M, Hansen E, Joss C, von Briel C, et al. Mediastinal lymph node clearance after docetaxel-cisplatin Neoadjuvant chemotherapy is prognostic of survival in patients with stage IIIA pN2 non-small-cell lung cancer: a multicenter phase II trial. J Clin Oncol. 2003; 21: 1752-9.
[27] Alvarado R, Yi M, Le-Petross H, Gilcrease M, Mittendorf EA, Bedrosian I, et al. The role for sentinel lymph node dissection after neoadjuvant chemotherapy in patients who present with node-positive breast cancer. Ann Surg Oncol. 2012; 19: 3177-84.

[28] Minchinton AI, Tannock IF. Drug penetration in solid tumours. Nat Rev Cancer. 2006; 6: 583-92.
[29] Dewhirst MW, Secomb TW. Transport of drugs from blood vessels to tumour tissue. Nat Rev Cancer. 2017; 17: 738-50.
[30] Li H, Li Y, Wang X, Hou Y, Hong X, Gong T, et al. Rational design of polymeric hybrid micelles to overcome lymphatic and intracellular delivery barriers in cancer immunotherapy. Theranostics. 2017; 7: 4383-98.
[31] Qin L, Zhang F, Lu X, Wei X, Wang J, Fang X, et al. Polymeric micelles for enhanced lymphatic drug delivery to treat metastatic tumors. J Control Release. 2013; 171: 133-42.
[32] Kataoka K, Harada A, Nagasaki Y. Block copolymer micelles for drug delivery: Design, characterization and biological significance. Adv Drug Deliver Rev. 2012; 64: 37-48.
[33] Wang S, Huang P, Chen XY. Hierarchical targeting strategy for enhanced tumor tissue accumulation/retention and cellular internalization. Adv Mater. 2016; 28: 7340-64.
[34] Han H, Valdeperez D, Jin Q, Yang B, Li Z, Wu Y, et al. Dual enzymatic reaction-assisted gemcitabine delivery systems for programmed pancreatic cancer therapy. ACS Nano. 2017; 11: 1281-91.
[35] Ruoslahti E. Peptides as targeting elements and tissue penetration devices for nanoparticles. Adv Mater. 2012; 24: 3747-56.
[36] Ji TJ, Ding YP, Zhao Y, Wang J, Qin H, Liu XM, et al. Peptide assembly integration of fibroblast-targeting and cell-penetration features for enhanced antitumor drug delivery. Adv Mater. 2015; 27: 1865-73.
[37] Nakase I, Konishi Y, Ueda M, Saji H, Futaki S. Accumulation of arginine-rich cell-penetrating peptides in tumors and the potential for anticancer drug delivery in vivo. J Control Release. 2012; 159: 181-8.
[38] Copolovici DM, Langel K, Eriste E, Langel U. Cell-penetrating peptides: design, synthesis, and applications. ACS Nano. 2014; 8: 1972-94.
[39] Cao HQ, Zou LL, He B, Zeng LJ, Huang YZ, Yu HJ, et al. Albumin biomimetic nanocorona improves tumor targeting and penetration for synergistic therapy of metastatic breast cancer. Adv Funct Mater. 2017; 27: 1605679.
[40] He B, Tan T, Wang H, Hu H, Wang Z, Wang J, et al. Rational design of tumor microenvironment-activated micelles for programed targeting of breast cancer metastasis. Adv Funct Mater. 2018; 28: 1705622.
[41] He XY, Bao XY, Cao HQ, Zhang ZW, Yin Q, Gu WW, et al. Tumor-penetrating nanotherapeutics loading a near-infrared probe inhibit growth and metastasis of breast cancer. Adv Funct Mater. 2015; 25: 2831-9.
[42] Wang J, Mao W, Lock LL, Tang J, Sui M, Sun W, et al. The role of micelle size in tumor accumulation, penetration, and treatment. ACS Nano. 2015; 9: 7195-206.
[43] Stylianopoulos T, Poh M-Z, Insin N, Bawendi MG, Fukumura D, Munn Lance L, et al. Diffusion of particles in the extracellular matrix: the effect of repulsive electrostatic interactions. Biophys J. 2010; 99: 1342-9.
[44] Lieleg O, Baumgärtel RM, Bausch AR. Selective filtering of particles by the extracellular matrix: an electrostatic bandpass. Biophys J. 2009; 97: 1569-77.
[45] Wang G, Chen Y, Wang P, Wang Y, Hong H, Li Y, et al. Preferential tumor accumulation and desirable interstitial penetration of poly(lactic-co-glycolic acid) nanoparticles with dual coating of chitosan oligosaccharide and polyethylene glycol-poly(d,l-lactic acid). Acta Biomater. 2016; 29: 248-60.
[46] Vrignaud P, Semiond D, Lejeune P, Bouchard H, Calvet L, Combeau C, et al. Preclinical antitumor activity of cabazitaxel, a semisynthetic taxane active in taxane-resistant tumors. Clin Cancer Res. 2013; 19: 2973-83.
[47] Chen J, Ding J, Wang Y, Cheng J, Ji S, Zhuang X, et al. Sequentially responsive shell-stacked nanoparticles for deep penetration into solid tumors. Adv Mater. 2017; 29: 1701170.
[48] Sun Q, Ojha T, Kiessling F, Lammers T, Shi Y. Enhancing tumor penetration of nanomedicines. Biomacromolecules. 2017; 18: 1449-59.
[49] Torok S, Rezeli M, Kelemen O, Vegvari A, Watanabe K, Sugihara Y, et al. Limited tumor tissue drug penetration contributes to primary resistance against angiogenesis inhibitors. Theranostics. 2017; 7: 400-12.
[50] Karaman S, Detmar M. Mechanisms of lymphatic metastasis. J Clin Invest. 2014; 124: 922-8.
[51] Yang X, Wang Z, Zhang F, Zhu G, Song J, Teng GJ, et al. Mapping sentinel lymph node metastasis by dual-probe optical imaging. Theranostics. 2017; 7: 153-63.
[52] Cao HQ, Dan ZL, He XY, Zhang ZW, Yu HJ, Yin Q, et al. Liposomes coated with isolated macrophage membrane can target lung metastasis of breast cancer. ACS Nano. 2016; 10: 7738-48.
[53] Cao HQ, Zhang ZW, Zhao S, He XY, Yu HJ, Yin Q, et al. Hydrophobic interaction mediating self-assembled nanoparticles of succinobucol suppress lung metastasis of breast cancer by inhibition of VCAM-1 expression. J Control Release. 2015; 205: 162-71.